



Hot Corinos Chemical Diversity: Myth or Reality?

Marta De Simone¹, Cecilia Ceccarelli¹, Claudio Codella^{1,2}, Brian E. Svoboda^{3,4}, Claire Chandler³, Mathilde Bouvier¹, Satoshi Yamamoto⁵, Nami Sakai⁶, Paola Caselli⁷, Cecile Favre¹, Laurent Loinard⁸, Bertrand Lefloch¹, Haiyu Baobab Liu⁹, Ana López-Sepulcre^{1,10}, Jaime E. Pineda⁷, Vianney Taquet², and Leonardo Testi^{2,11,12}

¹ Univ. Grenoble Alpes, CNRS, IPAG, F-38000 Grenoble, France; marta.desimone@univ-grenoble-alpes.fr

² INAF, Osservatorio Astrofisico di Arcetri, Largo E. Fermi 5, I-50125 Firenze, Italy

³ National Radio Astronomy Observatory, 1003 Lopezville Road, Socorro, NM 87801, USA

⁴ Steward Observatory, University of Arizona, 933 North Cherry Avenue, Tucson, AZ 85721, USA

⁵ Department of Physics, The University of Tokyo, Bunkyo-ku, Tokyo 113-0033, Japan

⁶ The Institute of Physical and Chemical Research (RIKEN), 2-1, Hirosawa, Wako-shi, Saitama 351-0198, Japan

⁷ Max-Planck-Institut für extraterrestrische Physik (MPE), Giessenbachstrasse 1, D-85748 Garching, Germany

⁸ Instituto de Radioastronomía y Astrofísica, Universidad Nacional Autónoma de México Apartado 58090, Morelia, Michoacán, Mexico

⁹ Academia Sinica Institute of Astronomy and Astrophysics (ASIAA), No. 1, Section 4, Roosevelt Road, Taipei 10617, Taiwan

¹⁰ Institut de Radioastronomie Millimétrique (IRAM), 300 rue de la Piscine, F-38400 Saint-Martin d'Hères, France

¹¹ ESO, Karl Schwarzschild Str. 2, D-85478 Garching bei München, Germany

¹² Excellence Cluster Origins, Boltzmannstrasse 2, D-85748 Garching bei München, Germany

Received 2020 April 7; revised 2020 April 22; accepted 2020 April 25; published 2020 June 8

Abstract

After almost 20 years of hunting, only about a dozen hot corinos, hot regions enriched in interstellar complex organic molecules (iCOMs), are known. Of them, many are binary systems with the two components showing drastically different molecular spectra. Two obvious questions arise. Why are hot corinos so difficult to find and why do their binary components seem chemically different? The answer to both questions could be a high dust opacity that would hide the molecular lines. To test this hypothesis, we observed methanol lines at centimeter wavelengths, where dust opacity is negligible, using the Very Large Array interferometer. We targeted the NGC 1333 IRAS 4A binary system, for which one of the two components, 4A1, has a spectrum deprived of iCOMs lines when observed at millimeter wavelengths, while the other component, 4A2, is very rich in iCOMs. We found that centimeter methanol lines are similarly bright toward 4A1 and 4A2. Their non-LTE analysis indicates gas density and temperature ($\geq 2 \times 10^6 \text{ cm}^{-3}$ and 100–190 K), methanol column density ($\sim 10^{19} \text{ cm}^{-2}$), and extent (~ 35 au in radius) similar in 4A1 and 4A2, proving that both are hot corinos. Furthermore, the comparison with previous methanol line millimeter observations allows us to estimate the optical depth of the dust in front of 4A1 and 4A2, respectively. The obtained values explain the absence of iCOMs line emission toward 4A1 at millimeter wavelengths and indicate that the abundances toward 4A2 are underestimated by $\sim 30\%$. Therefore, centimeter observations are crucial for the correct study of hot corinos, their census, and their molecular abundances.

Unified Astronomy Thesaurus concepts: [Interstellar medium \(847\)](#); [Protostars \(1302\)](#); [Star formation \(1569\)](#); [Chemical abundances \(224\)](#); [Astrochemistry \(75\)](#)

1. Introduction

Interstellar complex organic molecules (iCOMs) are molecules detected in the interstellar medium containing carbon and at least six atoms (Herbst & van Dishoeck 2009; Ceccarelli et al. 2017). These molecules are of particular interest because they carry a substantial fraction of carbon that can be used for prebiotic chemistry (e.g., Caselli & Ceccarelli 2012).

In solar-like young Class 0 protostars, iCOMs are found in relatively large quantities toward the so-called hot corinos, which are compact (≤ 100 au), hot (≥ 100 K), and dense ($\geq 10^7 \text{ cm}^{-3}$) regions enriched in iCOMs at the center of the envelopes accreting the future star (Ceccarelli 2004; Ceccarelli et al. 2007; Caselli & Ceccarelli 2012).

The first hot corino was discovered in 2003 toward the Class 0 source IRAS 16293–2422 (e.g., Cazaux et al. 2003; Jørgensen et al. 2016; Manigand et al. 2020). Since then other Class 0 hot corinos have been discovered: NGC 1333 IRAS 4A

(hereafter IRAS 4A; e.g., Bottinelli et al. 2004; Taquet et al. 2015; De Simone et al. 2017; López-Sepulcre et al. 2017; Sahu et al. 2019), NGC 1333 IRAS 2A, NGC 1333 IRAS 4B (e.g., Jørgensen et al. 2005; Bottinelli et al. 2007; Maury et al. 2014; De Simone et al. 2017), HH 212 (Codella et al. 2016; Bianchi et al. 2017; Lee et al. 2017, 2019), B335 (Imai et al. 2016), L483 (Oya et al. 2017; Jacobsen et al. 2019), Barnard1b-S (Marcelino et al. 2018), Ser-emb 1 (Martin-Domenech et al. 2019), and BHR71-IRS1 (Yang et al. 2020). Lately, a few more evolved Class I hot corinos were also discovered: NGC 1333 SVS13A (De Simone et al. 2017; Bianchi et al. 2019), B1a (Öberg et al. 2014), and Ser-emb 17 (Bergner et al. 2019). Therefore, after almost 20 years, only about a dozen hot corinos are known. Recent surveys concluded that $\sim 30\%$ of low-mass Class 0/I protostars show emission from at least three iCOMs (De Simone et al. 2017; Belloche et al. 2020).

Most of the hot corinos cited above turn out to be binary systems when imaged at high angular resolution. This is in agreement with previous surveys that found that 40–60% of protostars are multiple systems (Maury et al. 2014; Tobin et al. 2016). Interestingly, with the first hot corino maps it became

¹³ The National Radio Astronomy Observatory is a facility of the National Science Foundation operated under cooperative agreement by Associated Universities, Inc.

clear that the two objects in a given binary system can substantially differ in molecular complexity. Illustrative examples are provided by IRAS 16293–2422 and IRAS 4A (Jørgensen et al. 2016; López-Sepulcre et al. 2017). IRAS 16293–2422 is composed of two sources, A and B, separated by $5''.1$ (~ 720 au), where source A, weaker in millimeter continuum emission, is brighter in iCOMs lines than source B (e.g., Caux et al. 2011; Pineda et al. 2012; Jørgensen et al. 2016; Manigand et al. 2020). IRAS 4A, located in the NGC 1333 region in the Perseus cloud at a distance of (299 ± 15) pc (Zucker et al. 2018), is also a binary system composed of IRAS 4A1 and IRAS 4A2 (hereafter 4A1 and 4A2), separated by $1''.8$ (~ 540 au): while 4A1 is brighter in the millimeter continuum than 4A2, only 4A2 shows bright iCOMs lines (Taquet et al. 2015; De Simone et al. 2017; López-Sepulcre et al. 2017). However, not always the brightest millimeter continuum source in a binary system is the one weak iCOMs emission (see, e.g., Ospina-Zamudio et al. 2018).

In summary, despite two decades of hunting, only a dozen hot corinos are known so far. Of them, many are binary systems with the two components showing drastically different molecular spectra. Two related questions arise: (1) Why are hot corinos so difficult to find? While it is known that not all Class 0/I sources possess hot corinos (e.g., Sakai & Yamamoto 2013; Higuchi et al. 2018; Bouvier et al. 2020), observational biases might hamper their detection. (2) Why do coeval objects seem drastically different in their chemical composition? Is this a real difference or is it only/mostly due to observational biases?

A major observational bias could be caused by the dust opacity, which could be very high in Class 0/I sources, due to their high densities and, consequently, column densities (e.g., Miotello et al. 2014; Galván-Madrid et al. 2018; Galametz et al. 2019). If the effect of dust absorption is not negligible, there are three major consequences: (1) hot corinos may be difficult to detect in the millimeter (also) because of the high dust absorption of the iCOMs lines; (2) the molecular complexity diversity observed in binary system objects may reflect a difference in the front dust column density rather than a real chemical difference of the two objects; (3) the iCOM abundances in hot corinos could have been underestimated so far. In order to test this hypothesis, we targeted the IRAS 4A binary system, where the two objects show extremely different iCOM line spectra at millimeter wavelengths (see above), and carried out observations of several methanol lines, one of the simplest iCOMs, at centimeter wavelengths where the dust is optically thin.

2. Observations

The IRAS 4A system was observed at 1.3 cm using *K*-band receivers (18–26.5 GHz) of the Karl G. Jansky Very Large Array (VLA) in C-configuration (35–3400 m) on 2018 December 10 (project ID: VLA/18B-166). We targeted 10 CH_3OH lines, with frequencies from 24.9 to 26.4 GHz, upper level energies E_{up} from 36 to 175 K and Einstein coefficients A_{ij} in the range $(0.5\text{--}1.1) \times 10^{-7} \text{ s}^{-1}$ (Table 1). The observed spectra were divided into eight spectral windows with ~ 0.017 MHz (0.2 km s^{-1}) spectral resolution and $\sim 1''$ (~ 300 au at the distance of IRAS 4A) angular resolution. The observations were centered on 4A2, at $\alpha(\text{J2000}) = 03^{\text{h}}29^{\text{m}}10^{\text{s}}.43$, $\delta(\text{J2000}) = 31^{\circ}13'32''.1$. The flux calibrators were J0137+3309 and J0521+1638, while the bandpass and the gain

ones were J0319+4130 and J0336+3218, respectively. The absolute flux calibration error is $\leq 15\%$.¹⁴

The data reduction and cleaning process were performed using the CASA¹⁵ package while data analysis and images were performed using the GILDAS¹⁶ package. We obtained a continuum image by averaging line-free channels from all the spectral windows (Figure 1). We self-calibrated, in phase amplitude, using the line-free continuum channels and applied the solutions to both the continuum and molecular lines. The dynamic range, as defined by peak source flux over rms noise, was improved by 20% by the self-calibration. The final rms noise in the continuum image, $3 \mu\text{Jy beam}^{-1}$, is consistent with that reported by the VLA Exposure Time Calculator for a line-free continuum bandwidth of 4.5 GHz, 26 antennas, and an on-source integration time of 3 hr. The cube was subsequently continuum subtracted, smoothed to 1 km s^{-1} (~ 0.08 MHz), and cleaned in CASA using a multiscale deconvolution¹⁷ (scales = [0, 5, 15, 18, 25]) with natural weighting. The synthesized beams for each spectral window are reported in Table 1. The half power primary beam is $\sim 80''$.

3. Results

3.1. Continuum Emission Map

Figure 1 reports the map of the continuum emission at 25 GHz. The two continuum peaks mark the two protostars, whose coordinates ($\alpha(\text{J2000}) = 03^{\text{h}}29^{\text{m}}10^{\text{s}}.536$, $\delta(\text{J2000}) = 31^{\circ}13'31''.07$ for 4A1, and $\alpha(\text{J2000}) = 03^{\text{h}}29^{\text{m}}10^{\text{s}}.43$, $\delta(\text{J2000}) = 31^{\circ}13'32''.1$ for 4A2) are consistent with those derived by Tobin et al. (2016) and López-Sepulcre et al. (2017) with higher angular resolution observations. Since the angular resolution of our observations ($\sim 1''$) is smaller than the separation between 4A1 and 4A2 ($1''.8$), they are clearly disentangled in our images, even if individually unresolved with the current resolution.

At centimeter wavelengths, 4A1 shows a brighter continuum emission (due to dust or free-free) than 4A2. The peak fluxes are $(2.1 \pm 0.3) \text{ mJy beam}^{-1}$ and $(0.47 \pm 0.07) \text{ mJy beam}^{-1}$ toward 4A1 and 4A2, respectively. Taking into account the slightly different wavelength (1.05 cm) and angular resolution ($\sim 0''.1$), these values are consistent with the ones measured by Tobin et al. (2016): $(1.3 \pm 0.2) \text{ mJy beam}^{-1}$ for 4A1 and $(0.38 \pm 0.04) \text{ mJy beam}^{-1}$ for 4A2.

3.2. Methanol Lines

All the targeted methanol lines are detected with a signal-to-noise ratio larger than 3 (Table 1). Their velocity-integrated spatial distribution is shown in Figure 1. The methanol emission peaks exactly toward the 4A1 and 4A2 continuum peaks, and it is well disentangled, even if unresolved at the current angular resolution, around the two protostars.

Figure 2 shows the 10 methanol line spectra, isolated and not contaminated by other species, extracted toward the 4A1 and

¹⁴ <https://science.nrao.edu/facilities/vla/docs/manuals/oss/performance/fdscale>

¹⁵ <https://casa.nrao.edu/>

¹⁶ <http://www.iram.fr/IRAMFR/GILDAS>

¹⁷ This technique is a scale-sensitive deconvolution algorithm efficient for images with complicated and extended spatial structures. In fact, it allows us to model the sky brightness as a linear combination of flux components of different scale sizes. The scale sizes are chosen following approximately the sizes of the dominant structures in the image and including the “0” scale to model the unresolved ones (see [casadocs-deconvolution-algorithms](#)).

Table 1
Spectral Parameters, Synthesized Beams, and Gaussian Fit Results of the CH₃OH Lines Extracted toward the 4A1 and 4A2 Continuum Peaks

Transition	Frequency ^a (GHz)	E_{up}^{a} (K)	$\log A_{ij}^{\text{a}}$	Synthesized Beam maj \times min (PA) (" \times " (°))	IRAS 4A1				IRAS 4A2			
					$\int T_B dV^{\text{b}}$ (K km s ⁻¹)	$V_{\text{peak}}^{\text{b}}$ (km s ⁻¹)	FWHM ^b (km s ⁻¹)	rms ^c (K)	$\int T_B dV^{\text{b}}$ (K km s ⁻¹)	$V_{\text{peak}}^{\text{b}}$ (km s ⁻¹)	FWHM ^b (km s ⁻¹)	rms ^c (K)
3(2, 1)–3(1, 2) E	24.92871	36	–7.2	0.97 \times 0.95 (–12)	17(4)	6.5(0.2)	2.7(1.2)	1.0	34(3)	6.8(0.2)	3.1(0.3)	0.9
4(2, 2)–4(1, 3) E	24.93347	45	–7.1	0.97 \times 0.95 (–12)	23(3)	6.5(0.2)	3.7(0.5)	1.0	32(3)	6.9(0.2)	3.1(0.3)	0.9
2(2, 0)–2(1, 1) E	24.93438	29	–7.2	0.97 \times 0.95 (–12)	19(3)	6.5(0.2)	3.3(0.6)	1.0	27(3)	6.9(0.2)	2.9(0.3)	0.9
5(2, 3)–5(1, 4) E	24.95908	57	–7.1	0.97 \times 0.95 (–12)	19(3)	6.1(0.3)	4.2(0.9)	0.9	32(3)	6.8(0.2)	3.1(0.3)	0.9
6(2, 4)–6(1, 5) E	25.01812	71	–7.1	0.97 \times 0.95 (–19)	19(3)	6.3(0.3)	3.5(0.6)	1.0	31(3)	6.7(0.1)	2.5(0.2)	1.0
7(2, 5)–7(1, 6) E	25.12487	87	–7.1	0.98 \times 0.95 (–21)	20(2)	7.0(0.2)	3.2(0.5)	0.9	35(3)	6.8(0.2)	2.9(0.3)	1.2
8(2, 6)–8(1, 7) E	25.29442	106	–7.0	0.96 \times 0.94 (–11)	13(3)	6.8(0.3)	3.4(0.9)	0.9	32(2)	6.8(0.1)	2.8(0.3)	0.9
9(2, 7)–9(1, 8) E	25.54140	127	–7.0	0.96 \times 0.92 (–50)	18(2)	6.5(0.2)	2.7(0.5)	0.8	31(2)	6.9(0.1)	2.6(0.2)	0.9
10(2, 8)–10(1, 9) E	25.87827	150	–7.0	0.97 \times 0.93 (–35)	20(2)	6.4(0.2)	3.2(0.5)	0.8	32(2)	6.9(0.1)	2.6(0.2)	0.8
11(2, 9)–11(1, 10) E	26.31312	175	–6.9	0.94 \times 0.91 (–35)	24(4)	6.0(0.4)	4.9(0.9)	1.1	31(3)	6.8(0.1)	2.9(0.3)	0.9

Notes.

^a Spectroscopic parameters by Xu et al. (2008) are from the Cologne Database for Molecular Spectroscopy (Müller et al. 2005).

^b Results of the Gaussian fit algorithm.

^c The rms is computed over each spectral window.

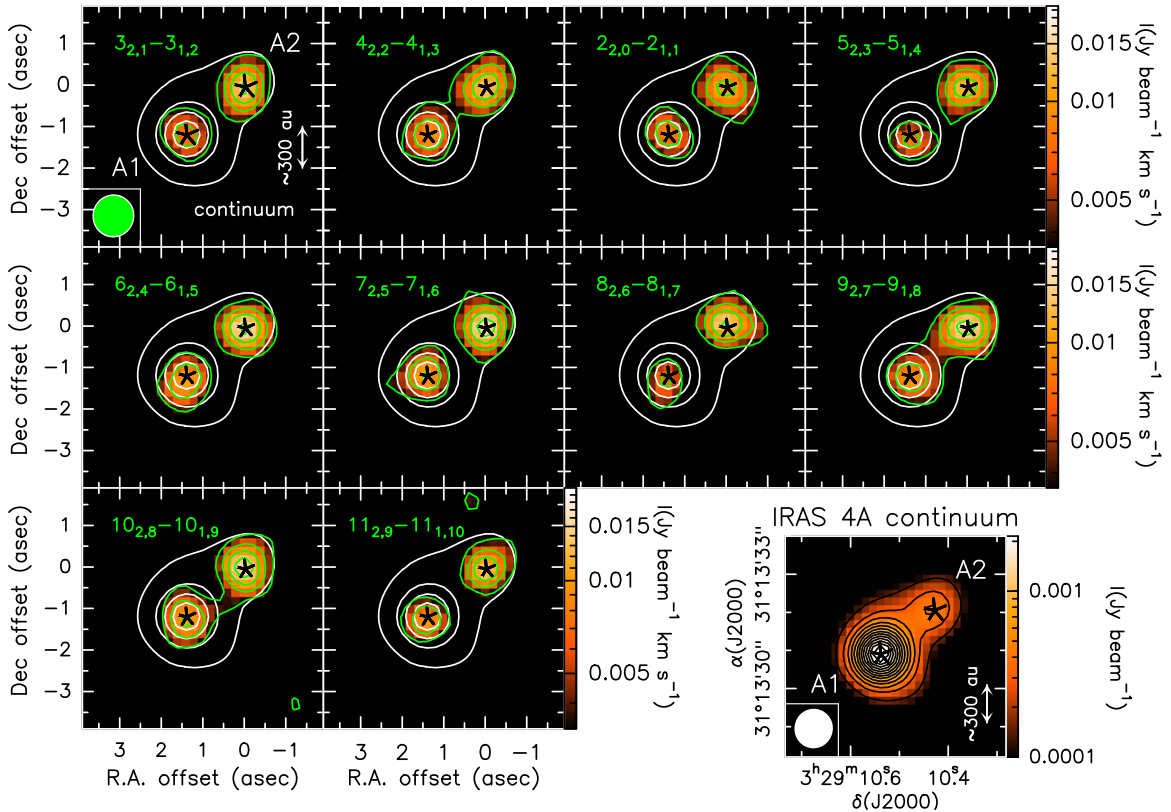
CH₃OH – NGC 1333 IRAS 4A

Figure 1. Bottom right panel: IRAS 4A continuum emission map at 25 GHz. First contour and steps correspond to $50\sigma_C$ ($\sigma_C = 3 \mu\text{Jy beam}^{-1}$). Other panels: CH₃OH velocity-integrated maps toward IRAS 4A in color scale overlapped with the continuum (white) contours (from $50\sigma_C$ with steps of $170\sigma_C$). The emission is integrated from -2 to 2 km s^{-1} with respect to the v_{sys} ($\sim 6.7 \text{ km s}^{-1}$). Methanol first contour (green) and steps correspond to 3σ ($\sigma = 1.2 \text{ mJy beam}^{-1} \text{ km s}^{-1}$). The transition of the imaged line is reported in each panel. The black stars show the 4A1 and 4A2 positions. Synthesized beams for continuum (white) and lines (green) are in the lower left corner.

4A2 continuum peaks. The lines are slightly brighter toward 4A2 than 4A1, whereas the linewidths are very similar (see also Table 1). We derived the velocity-integrated line intensities for each detected CH₃OH transition using a Gaussian fit, being the profile Gaussian-like. The fit results for both sources, namely the integrated emission ($\int T_b dV$), the linewidth (FWHM), the peak velocities (V_{peak}), and the rms computed for each spectral window, are reported in Table 1. The velocity peaks are consistent with the systemic velocity of the molecular envelope surrounding IRAS 4A ($\sim 6.7 \text{ km s}^{-1}$; Choi 2001). The linewidths are between 3 and 4 km s^{-1} in agreement with those found by Taquet et al. (2015) and López-Sepulcre et al. (2017) toward 4A2 at millimeter wavelength.

In summary, our new VLA observations show a first clear important result: the detection of methanol emission toward 4A1, the protostar where previous millimeter observations showed no iCOMs emission (López-Sepulcre et al. 2017).

4. Centimeter versus Millimeter Observations: Dust Absorption Derivation

We compared our new centimeter observations of methanol lines with previous ones at 143–146 GHz in order to understand whether the dust absorption, more important at millimeter than at centimeter wavelengths, may explain the absence of iCOM millimeter line emission in 4A1 (López-Sepulcre et al. 2017). We first carried out a non-LTE analysis of the centimeter methanol lines from which we derived the gas

temperature, density and CH₃OH column density toward 4A1 and 4A2 (Section 4.1). Then, using the same parameters, we predicted the methanol line intensities at 143–146 GHz, the frequency of the observations by Taquet et al. (2015; Section 4.2). Finally, we compared the predicted and measured millimeter line intensities and we attributed the difference to the absorption of the dust between us and the gas emitting methanol, via the usual equation:

$$I_\nu^{\text{obs}} = I_\nu^{\text{pred}} e^{-\tau_\nu} \quad (1)$$

in order to derive the dust optical depth toward 4A1 and 4A2, respectively (Section 4.3). Please note that the foreground dust opacity obtained by Equation (1) assumes that the absorbing dust fully covers the emitting gas area, which may not necessarily be the case. Yet, the derived attenuation of the methanol line intensities is still valid, even though it is only an average over the emitting gas area.

4.1. Non-LTE Analysis of the Centimeter Methanol Lines

To derive the physical properties of the gas emitting CH₃OH, namely gas temperature, density and methanol column density, we performed a non-LTE analysis using a Large Velocity Gradient (LVG) code (Ceccarelli et al. 2003). CH₃OH can be identified in A- and E-type due to the total spin (I) state of the hydrogen nuclei in the CH₃ group: A-type if the total spin function is symmetric ($I = 3/2$), E-type if

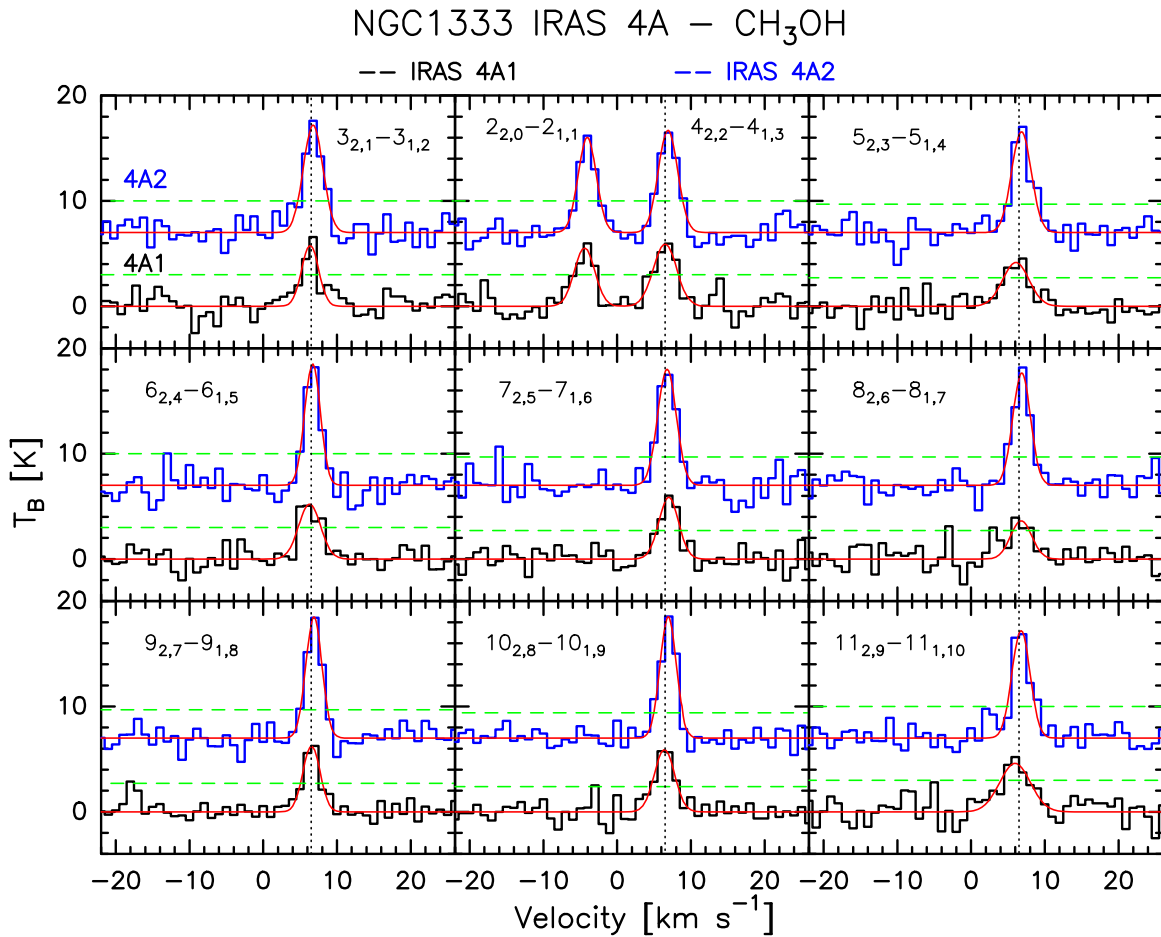


Figure 2. Methanol lines (marked in each panel) detected in the VLA *K*-band toward 4A1 (black) and 4A2 (blue). The horizontal green dashed lines show the 3σ level. The vertical dotted black lines report the v_{sys} (6.7 km s^{-1}). The red and magenta curves show the best Gaussian fits (see Table 1).

asymmetric ($I = 1/2$) (Rabli & Flower 2010). We used the collisional coefficients of both types of CH₃OH with para-H₂, computed by Rabli & Flower (2010) between 10 and 200 K for the first 256 levels and provided by the BASECOL database (Dubernet et al. 2013). We assumed a spherical geometry to compute the line escape probability (de Jong et al. 1980), the CH₃OH-A/CH₃OH-E ratio equal to 1, the H₂ ortho-to-para ratio equal to 3, and that the levels are populated by collisions and not by the absorption of the dust background photons whose contribution is very likely negligible due to the low values of the CH₃OH Einstein coefficients A_{ij} . Please note that the present LVG analysis only accounts for the line optical depth (to have also the dust τ in the methanol emitting region would require information on the structure of the region that we do not have, as the emission is unresolved).

We ran a large grid of models ($\geq 10,000$) covering the frequency of the observed lines, a total (CH₃OH-A plus CH₃OH-E) column density $N_{\text{CH}_3\text{OH}}$ from 2×10^{16} to $8 \times 10^{19} \text{ cm}^{-2}$, a gas density n_{H_2} from 1×10^6 to $2 \times 10^8 \text{ cm}^{-3}$, and a temperature T from 80 to 200 K. We then simultaneously fitted the measured CH₃OH-A and CH₃OH-E line intensities via comparison with those simulated by the LVG model, leaving $N_{\text{CH}_3\text{OH}}$, n_{H_2} , T , and the emitting size θ as free parameters. Following the observations, we assumed the linewidths equal to 3.5 km s^{-1} and 3.0 km s^{-1} for 4A1 and

4A2, respectively, and we included the calibration uncertainty (15%) in the observed intensities.

The best fit is obtained for a total CH₃OH column density $N_{\text{CH}_3\text{OH}} = 2.8 \times 10^{19} \text{ cm}^{-2}$ with reduced chi-square $\chi_R^2 = 0.6$ for 4A1 and $N_{\text{CH}_3\text{OH}} = 1 \times 10^{19} \text{ cm}^{-2}$ with $\chi_R^2 = 0.1$ for 4A2. All the observed lines are predicted to be optically thick and emitted by a source of $0''22$ for 4A1 and $0''24$ for 4A2 ($\sim 70 \text{ au}$) in diameter. Solutions with $N_{\text{CH}_3\text{OH}} \geq 1 \times 10^{18} \text{ cm}^{-2}$ for 4A2 and $\geq 1 \times 10^{19} \text{ cm}^{-2}$ for 4A1 are within 1σ of confidence level. Increasing the methanol column density, the χ_R^2 decreases until it reaches a constant value for $N_{\text{CH}_3\text{OH}} \geq 1 \times 10^{19} \text{ cm}^{-2}$ for 4A1 and $N_{\text{CH}_3\text{OH}} \geq 3 \times 10^{19} \text{ cm}^{-2}$ for 4A2; this is because all the observed lines become optically thick ($\tau \sim 10\text{--}30$ for 4A1, $\tau \sim 2\text{--}6$ for 4A2) and, consequently, the emission becomes that of a blackbody. The results do not change assuming a linewidth $\pm 0.5 \text{ km s}^{-1}$ with respect to the chosen one.

Figure 3 shows, for both sources, the density-temperature χ^2 surface of the $N_{\text{CH}_3\text{OH}}$ best fit. The gas temperature is (90–130) K for 4A1 and (120–190) K for 4A2, while for the gas density we obtained a lower limit of $2 \times 10^6 \text{ cm}^{-3}$ for 4A1 and $1.5 \times 10^7 \text{ cm}^{-3}$ for 4A2, which implies that the levels are LTE populated. The fit results are reported in Table 2. The derived n_{H_2} and T are consistent with those computed with the model summarized in Su et al. (2019) using our sizes.

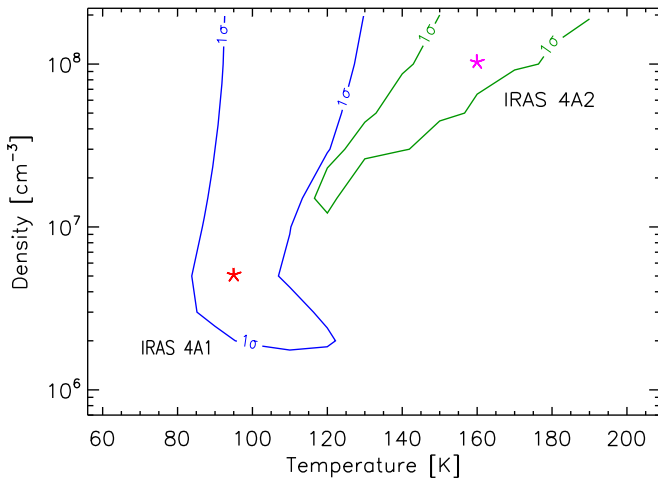


Figure 3. Density–temperature χ^2 contour plots. The contours represent 1σ confidence level contours for 4A1 (blue) and 4A2 (green), respectively, assuming the best-fit values of $N_{\text{CH}_3\text{OH}}$ and θ in Table 2. The best-fit solutions are marked by the red (4A1) and magenta (4A2) asterisks.

4.2. Predictions of Millimeter Methanol Line Intensities

Adopting the 1σ range of gas temperature and density derived for 4A1 and 4A2 (Table 2), we ran a new grid of LVG models with the CH_3OH column density from 1×10^{18} to $8 \times 10^{19} \text{ cm}^{-2}$ at 143–146 GHz to predict the methanol line intensities observed by Taquet et al. (2015). We then used the CH_3OH $3_1 - 2_1 \text{ A}^+$ line at 143.866 GHz, which provides the most stringent constraint to the dust optical depth, to compare the predicted intensity with that observed by Taquet et al. (2015). In the comparison, we took into account our LVG-derived source size and the angular resolution of the Taquet et al. (2015) observations. While for 4A2 we considered the line intensity quoted by Taquet et al. (2015), for 4A1, not having CH_3OH detection, we used the 3σ level of the Taquet et al. (2015) observations integrated over 3 km s^{-1} (average linewidth toward 4A1: see Section 3).

The 4A1 and 4A2 CH_3OH predicted and observed values are reported in Table 2. While the two intensities are similar toward 4A2, they differ by about a factor five toward 4A1.

4.3. Dust Absorption Toward 4A1 and 4A2

Assuming that the difference between the predicted and observed intensities is due to the (foreground) dust absorption and using Equation (1), we derived the dust optical depth at 143 GHz ($\tau_{\text{dust}}^{143\text{GHz}}$; Table 2). While $\tau_{\text{dust}}^{143\text{GHz}}$ toward 4A2 is small (~ 0.3), that toward 4A1 is large (≥ 1.6) enough to attenuate the methanol line intensity by a factor ≥ 5 . Therefore, the dust is affecting the millimeter line emission differently in the two sources.

5. Discussion

5.1. Is IRAS 4A1 a Hot Corino?

So far, only about a dozen hot corinos have been detected (Section 1) and the question arises whether this is because they are rare or because the searches have always been carried out at millimeter wavelengths, where dust could heavily absorb the line emission.

Our first result is that a source that was not supposed to be a hot corino based on millimeter observations, IRAS 4A1

(López-Sepulcre et al. 2017), indeed possesses a region with temperature $\geq 100 \text{ K}$ (Section 3), namely the icy mantle sublimation one, and shows methanol emission (Section 3), the simplest of the iCOMs, when observed at centimeter wavelengths. According to its definition (Ceccarelli 2004), thus, IRAS 4A1 is a hot corino.

Although we cannot affirm that hot corinos are ubiquitous, it is clear that the searches at millimeter wavelengths may be heavily biased and that complementary centimeter observations are necessary to account for dust opacity and understand the occurrence of hot corinos.

5.2. 4A2 versus 4A1: Are They Chemically Different?

Unlike 4A2, no sign of iCOM millimeter emission was revealed toward 4A1 (Taquet et al. 2015; López-Sepulcre et al. 2017). Using ALMA observations at 250 GHz, López-Sepulcre et al. (2017) found that the iCOMs abundances toward 4A2 and 4A1 differ by more than a factor 17, with the largest values (~ 100) for HCOOCH_3 and CH_3CN .

The first question to answer is whether the chemical difference between the two coeval objects is real or due to a different absorption by the surrounding dust.

In Section 4.3, we found that τ_{dust} at 143 GHz toward 4A1 and 4A2 is ≥ 1.6 and 0.3, respectively (see Table 2). Using the dependence of τ_{dust} from the frequency ($\tau_{\nu_2}/\tau_{\nu_1} = (\nu_2/\nu_1)^\beta$) and assuming $\beta = 2$ (ISM value), the optical depth scaled at 250 GHz (frequency at which López-Sepulcre et al. 2017, derived the above iCOMs abundance ratios) is ≥ 4.9 for 4A1 and 0.9 for 4A2. Therefore, the different dust absorption toward 4A1 and 4A2 provides us, as a lower limit, a factor of 55 difference in their line intensities (I^{A2}/I^{A1}), comparable to the 4A2/4A1 iCOMs abundance ratios derived by López-Sepulcre et al. (2017). A large dust absorption was also suggested by the anomalous flattened continuum spectral index at 100–230 GHz (Li et al. 2017) and the 90° flipping of the linear polarization position angles observed at above and below 100 GHz frequencies (Ko et al. 2020).

Although we cannot exclude that a real chemical difference exists between 4A1 and 4A2, the observations so far available cannot support that hypothesis. Centimeter observations of other iCOMs than methanol are necessary to settle this issue. This conclusion may apply to other binary systems where an apparent chemical difference is observed using millimeter observations.

5.3. Are the iCOM Abundances in Hot Corinos Underestimated?

The dust absorption also affects the iCOM line intensities in 4A2. At 143 GHz τ_{dust} is 0.3, which leads to underestimate the iCOM abundances by about 30%. At higher frequencies, this factor becomes more important; e.g., at 250 GHz, where several hot corinos studies are carried out (see references in Section 1), the absorption factor would be 2.5, and at 350 GHz, frequency where the most sensitive iCOMs search has been carried out (e.g., Jørgensen et al. 2016), the absorption factor would be 6. This behavior also agrees with what has already been found in massive hot cores (e.g., Rivilla et al. 2017). Therefore, in order to derive reliable iCOM abundances, complementary centimeter observations are needed to estimate the dust absorption.

Table 2
Top: Best-fit Results and 1σ Confidence Level (range) from the Non-LTE LVG Analysis of the CH₃OH Lines toward 4A1 and 4A2

		IRAS 4A1		IRAS 4A2	
		LVG Results			
		Best Fit	Range	Best Fit	Range
$n(\text{H}_2)$	(cm ⁻³)	5×10^6	$\geq 2 \times 10^6$	1×10^8	$\geq 1 \times 10^7$
T_{kin}	(K)	100	90–130	160	120–190
$N_{\text{CH}_3\text{OH}}$	(cm ⁻²)	2.4×10^{19}	$\geq 1 \times 10^{19}$	1×10^{19}	$\geq 1 \times 10^{18}$
Source size	($''$)	0.22	0.20–0.24	0.24	0.22–0.30
Predictions versus Millimeter Observations					
$T_b dV_{\text{pred}}$	(K km s ⁻¹)	4.7(0.8)		9.1(1.2)	
$T_b dV_{\text{obs}}$	(K km s ⁻¹)	≤ 0.9		6.5(1.9)	
$\tau_{143\text{GHz}}^{\text{dust}}$		≥ 1.6		0.3	

Note. Bottom: Comparison of the LVG model predictions with the Taquet et al. (2015) millimeter observations (see the text).

6. Conclusion

We carried out observations of methanol lines at centimeter wavelengths with the VLA interferometer toward the binary system IRAS 4A, where previous millimeter observations showed a possible chemical differentiation between the two objects. Specifically, while 4A2 showed iCOM line emission, 4A1 did not.

Our new observations detected 10 methanol lines in 4A1 and 4A2 with similar intensities. Using a non-LTE analysis and comparing with previous methanol millimeter observations, we showed that (1) 4A1 is a hot corino, (2) the lack of iCOMs detection toward 4A1 at millimeter wavelengths is caused by a large dust optical depth, and (3) the determination of the iCOMs abundances toward 4A2 via millimeter observations is slightly underestimated by the dust absorption.


Therefore, the difficulty in discovering new hot corinos could be because the searches have been carried out at (sub) millimeter wavelengths, where the dust absorption might not be negligible. The suspected different chemical nature of coeval objects of the same binary system needs also to be verified at centimeter wavelengths, as well as the iCOM abundances estimated from millimeter observations.

We conclude that centimeter observations of hot corinos are of paramount importance for their correct study. In the future, next generation instruments in the centimeter wavelength regime, such as ngVLA (McGuire et al. 2018) and SKA (Codella et al. 2015), could be the most efficient way to identify hot corinos and certainly the most appropriate facilities to study them.

We thank the referee P.T.P Ho for his fruitful comments and suggestions. This work has received funding from the European Research Council (ERC) under the European Union’s Horizon 2020 research and innovation programme, for the Project “The Dawn of Organic Chemistry” (DOC), grant agreement No 741002. It was supported by the project PRIN-INAF 2016 The Cradle of Life–GENESIS-SKA (General Conditions in Early Planetary Systems for the rise of life with SKA), and partly supported by the Italian Ministero dell’Istruzione, Università e Ricerca, through the grant Progetti Premiali 2012–iALMA (CUP C52I13000140001). H.B.L. is supported by the Ministry of Science and Technology (MoST) of Taiwan (grant Nos. 108-2112-M-001-002-MY3). C.F. acknowledges support from the French National Research

Agency in the framework of the Investissements d’Avenir program (ANR-15-IDEX-02), through the funding of the “Origin of Life” project of the Univ. Grenoble-Alpes.

ORCID iDs

Marta De Simone  <https://orcid.org/0000-0001-5659-0140>
 Cecilia Ceccarelli  <https://orcid.org/0000-0001-9664-6292>
 Claudio Codella  <https://orcid.org/0000-0003-1514-3074>
 Brian E. Svoboda  <https://orcid.org/0000-0002-8502-6431>
 Claire Chandler  <https://orcid.org/0000-0002-7570-5596>
 Mathilde Bouvier  <https://orcid.org/0000-0003-0167-0746>
 Satoshi Yamamoto  <https://orcid.org/0000-0002-9865-0970>
 Nami Sakai  <https://orcid.org/0000-0002-3297-4497>
 Paola Caselli  <https://orcid.org/0000-0003-1481-7911>
 Cecile Favre  <https://orcid.org/0000-0002-5789-6931>
 Laurent Loinard  <https://orcid.org/0000-0002-5635-3345>
 Bertrand Lefloch  <https://orcid.org/0000-0002-9397-3826>
 Hauyu Baobab Liu  <https://orcid.org/0000-0003-2300-2626>
 Ana López-Sepulcre  <https://orcid.org/0000-0002-6729-3640>
 Jaime E. Pineda  <https://orcid.org/0000-0002-3972-1978>
 Vianney Taquet  <https://orcid.org/0000-0003-0407-7489>
 Leonardo Testi  <https://orcid.org/0000-0003-1859-3070>

References

- Belloche, A., Maury, A. J., Maret, S., et al. 2020, *A&A*, **635**, A198
 Bergner, J. B., Martín-Doménech, R., Öberg, K. I., et al. 2019, *ESC*, **3**, 1564
 Bianchi, E., Codella, C., Ceccarelli, C., et al. 2017, *A&A*, **606**, L7
 Bianchi, E., Codella, C., Ceccarelli, C., et al. 2019, *MNRAS*, **483**, 1850
 Bottinelli, S., Ceccarelli, C., Lefloch, B., et al. 2004, *ApJ*, **615**, 354
 Bottinelli, S., Ceccarelli, C., Williams, J. P., & Lefloch, B. 2007, *A&A*, **463**, 601
 Bouvier, M., López-Sepulcre, A., Ceccarelli, C., et al. 2020, *A&A*, **636**, A19
 Caselli, P., & Ceccarelli, C. 2012, *A&ARv*, **20**, 56
 Caux, E., Kahane, C., Castets, A., et al. 2011, *A&A*, **532**, A23
 Cazaux, S., Tielens, A. G. G. M., Ceccarelli, C., et al. 2003, *ApJL*, **593**, L51
 Ceccarelli, C. 2004, in ASP Conf. Proc. 323, Star Formation in the Interstellar Medium: In Honor of David Hollenbach, Chris McKee and Frank Shu, ed. D. Johnstone et al. (San Francisco, CA: ASP), 195
 Ceccarelli, C., Caselli, P., Fontani, F., et al. 2017, *ApJ*, **850**, 176
 Ceccarelli, C., Caselli, P., Herbst, E., Tielens, A. G. G. M., & Caux, E. 2007, in Protostars and Planets V, ed. B. Reipurth, D. Jewitt, & K. Keil (Tucson, AZ: Univ. Arizona Press), 47
 Ceccarelli, C., Maret, S., Tielens, A. G. G. M., Castets, A., & Caux, E. 2003, *A&A*, **410**, 587
 Choi, M. 2001, *ApJ*, **553**, 219
 Codella, C., Ceccarelli, C., Cabrit, S., et al. 2016, *A&A*, **586**, L3

- Codella, C., Podio, L., Fontani, F., et al. 2015, *Advancing Astrophysics with the Square Kilometre Array (AASKA14) (Sissa: POS)*, 123
- de Jong, T., Boland, W., & Dalgarno, A. 1980, *A&A*, 91, 68
- De Simone, M., Codella, C., Testi, L., et al. 2017, *A&A*, 599, A121
- Dubernet, M.-L., Alexander, M. H., Ba, Y. A., et al. 2013, *A&A*, 553, A50
- Galametz, M., Maury, A. J., Valdivia, V., et al. 2019, *A&A*, 632, A5
- Galván-Madrid, R., Liu, H. B., Izquierdo, A. F., et al. 2018, *ApJ*, 868, 39
- Herbst, E., & van Dishoeck, E. F. 2009, *ARA&A*, 47, 427
- Higuchi, A. E., Sakai, N., Watanabe, Y., et al. 2018, *ApJS*, 236, 52
- Imai, M., Sakai, N., Oya, Y., et al. 2016, *ApJL*, 830, L37
- Jacobsen, Jørgensen, Jes, K., Di Francesco, James, et al. 2019, *A&A*, 629, A29
- Jørgensen, J. K., Bourke, T. L., Myers, P. C., et al. 2005, *ApJ*, 632, 973
- Jørgensen, J. K., van der Wiel, M. H. D., Coutens, A., et al. 2016, *A&A*, 595, A117
- Ko, C.-L., Liu, H. B., Lai, S.-P., et al. 2020, *ApJ*, 889, 172
- Lee, C.-F., Codella, C., Li, Z.-Y., & Liu, S.-Y. 2019, *ApJ*, 876, 63
- Lee, C.-F., Li, Z.-Y., Ho, P. T. P., et al. 2017, *ApJ*, 843, 27
- Li, J. I.-H., Liu, H. B., Hasegawa, Y., & Hirano, N. 2017, *ApJ*, 840, 72
- López-Sepulcre, A., Sakai, N., Neri, R., et al. 2017, *A&A*, 606, A121
- Manigand, S., Jørgensen, J. K., Calcutt, H., et al. 2020, *A&A*, 635, A48
- Marcelino, N., Gerin, M., Cernicharo, J., et al. 2018, *A&A*, 620, A80
- Martin-Domenech, R., Oberg, K. I., Bergner, J. B., & Jørgensen, J. K. 2019, *ApJ*, 880, 130
- Maury, A. J., Belloche, A., André, P., et al. 2014, *A&A*, 563, L2
- McGuire, B. A., Carroll, P. B., & Garrod, R. T. 2018, arXiv:1810.06586
- Miotello, A., Testi, L., Lodato, G., et al. 2014, *A&A*, 567, A32
- Müller, H. S. P., Schlöder, F., Stutzki, J., & Winnewisser, G. 2005, *JMoSt*, 742, 215
- Öberg, K. I., Lauck, T., & Graninger, D. 2014, *ApJ*, 788, 68
- Ospina-Zamudio, J., Lefloch, B., Ceccarelli, C., et al. 2018, *A&A*, 618, A145
- Oya, Y., Sakai, N., Watanabe, Y., et al. 2017, *ApJ*, 837, 174
- Pineda, J. E., Maury, A. J., Fuller, G. A., et al. 2012, *A&A*, 544, L7
- Rabli, D., & Flower, D. R. 2010, *MNRAS*, 406, 95
- Rivilla, V. M., Beltrán, M. T., Cesaroni, R., et al. 2017, *A&A*, 598, A59
- Sahu, D., Liu, S.-Y., Su, Y.-N., et al. 2019, *ApJ*, 872, 196
- Sakai, N., & Yamamoto, S. 2013, *ChRv*, 113, 8981
- Su, Y.-N., Liu, S.-Y., Li, Z.-Y., et al. 2019, *ApJ*, 885, 98
- Taquet, V., López-Sepulcre, A., Ceccarelli, C., et al. 2015, *ApJ*, 804, 81
- Tobin, J. J., Looney, L. W., Li, Z.-Y., et al. 2016, *ApJ*, 818, 73
- Xu, L.-H., Fisher, J., Lees, R., et al. 2008, *JMoSp*, 251, 305
- Yang, Y.-L., Evans, N. J., II, Smith, A., et al. 2020, *ApJ*, 891, 61
- Zucker, C., Schlafly, E. F., Speagle, J. S., et al. 2018, *ApJ*, 869, 83